

Article

In Situ Polycondensation Synthesis of NiS-g-C₃N₄ Nanocomposites for Catalytic Hydrogen Generation from NaBH₄

Alhulw H. Alshammari *^{ID}, Khulaif Alshammari, Turki Alotaibi, Majed Alshammari, Sultan Alhassan and Taha Abdel Mohaymen Taha ^{ID}

Physics Department, College of Science, Jouf University, Sakaka P.O. Box 2014, Saudi Arabia

* Correspondence: ahalshammari@ju.edu.sa

Abstract: The nanocomposites of S@g-C₃N₄ and NiS-g-C₃N₄ were synthesized for catalytic hydrogen production from the methanolysis of sodium borohydride (NaBH₄). Several experimental methods were applied to characterize these nanocomposites such as X-ray diffraction (XRD), Fourier transform infrared spectroscopy (FTIR), and environmental scanning electron microscopy (ESEM). The calculation of NiS crystallites revealed an average size of 8.0 nm. The ESEM and TEM images of S@g-C₃N₄ showed a 2D sheet structure and NiS-g-C₃N₄ nanocomposites showed the sheet materials that were broken up during the growth process, revealing more edge sites. The surface areas were 40, 50, 62, and 90 m²/g for S@g-C₃N₄, 0.5 wt.% NiS, 1.0 wt.% NiS, and 1.5 wt.% NiS, respectively. The pore volume of S@g-C₃N₄ was 0.18 cm³, which was reduced to 0.11 cm³ in 1.5 wt.% NiS owing to the incorporation of NiS particles into the nanosheet. We found that the in situ polycondensation preparation of S@g-C₃N₄ and NiS-g-C₃N₄ nanocomposites increased the porosity of the composites. The average values of the optical energy gap for S@g-C₃N₄ were 2.60 eV and decreased to 2.50, 2.40, and 2.30 eV as the NiS concentration increased from 0.5 to 1.5 wt.%. All NiS-g-C₃N₄ nanocomposite catalysts had an emission band that was visible in the 410–540 nm range and the intensity of this peak decreased as the NiS concentration increased from 0.5 to 1.5 wt.%. The hydrogen generation rates increased with increasing content of NiS nanosheet. Moreover, the sample 1.5 wt.% NiS showed the highest production rate of 8654 mL/g·min due to the homogeneous surface organization.

Keywords: carbon nitride; NiS; hydrogen energy; methanolysis; NaBH₄



Citation: Alshammari, A.H.; Alshammari, K.; Alotaibi, T.; Alshammari, M.; Alhassan, S.; Taha, T.A.M. In Situ Polycondensation Synthesis of NiS-g-C₃N₄ Nanocomposites for Catalytic Hydrogen Generation from NaBH₄. *Nanomaterials* **2023**, *13*, 938. <https://doi.org/10.3390/nano13050938>

Academic Editor: Antonio Guerrero-Ruiz

Received: 9 February 2023

Revised: 27 February 2023

Accepted: 2 March 2023

Published: 5 March 2023



Copyright: © 2023 by the authors. Licensee MDPI, Basel, Switzerland. This article is an open access article distributed under the terms and conditions of the Creative Commons Attribution (CC BY) license (<https://creativecommons.org/licenses/by/4.0/>).

1. Introduction

Research on graphitic carbon nitride (g-C₃N₄) has received a lot of attention due to its structure and substantial chemical and physical characteristics, such as superior electrical conductivity and high mechanical strength [1–3]. Moreover, the use of g-C₃N₄ in photocatalysis, electrocatalysis, photovoltaic devices, and bioimaging applications has a lot of potential [4–6]. It is composed of several abundant elements and is the most stable allotrope of carbon nitrides under ambient conditions. Graphite and g-C₃N₄ have a similar structure, however one by one, nitrogen and carbon atoms make up the hexatomic ring. A significant planer network structure is developed by the covalent connections that are formed by each carbon atom with three nitrogen atoms. The sp² hybridized C and N atoms are organized in a six-member stalked ring; providing the semiconductor properties of g-C₃N₄. In the optical range of 260–320 nm, g-C₃N₄ has a significant UV–Vis absorption peak. The π–π* electron transfer for g-C₃N₄ with s-triazine rings is responsible for the absorption peak, which is located at about 250 nm. Moreover, the n–π* electron transfer involving a lone pair of electrons on nitrogen atoms in the g-C₃N₄ produced the absorption peak at 320 nm [7,8]. The electrical features and surface chemical properties of g-C₃N₄ doped with heteroatoms (such as oxygen, sulfur, phosphorous, and boron) can be tuned, which is advantageous for expanding their applications in bioimaging and biosensing. For

catalytic usage, g-C₃N₄ has enhanced thermal stability because of higher durability and non-volatility up to 600 °C even in the air, according to the thermogravimetric analysis [8–10]. However, the limited solubility of g-C₃N₄ in organic solvents resists the processing of this material.

There is a potential use for metal sulfides in a variety of industries, including supercapacitors, catalysis, energy conversion, and biomedicine [11,12]. Due to their many structural forms, several metal sulfides have been investigated and widely used. Metal sulfide nanoparticle applications are influenced by characteristics including size, shape, surface area, and morphology. A well-known metal sulfide called nickel sulfide has been suggested as a promising material because of its nontoxicity, abundant mineral resources, and high stability for various energy storage and energy conversion applications [13,14]. The metallic structure of NiS provides high electrical conductivity, and this high conductivity enhances interfacial charge transfer and carrier separation. In order to facilitate interfacial charge transfer and separation, the NiS catalyst can serve as an electron-trapping agent and a site for the generation of H₂. Nanoscale nickel sulfide with a specified surface charge and functionality may be of interest for catalytic applications [15]. As a result, it is crucial to develop a precise preparation approach to couple nickel sulfides with the g-C₃N₄ nanosheet. Accordingly, the nanocomposite of NiS/g-C₃N₄ is expected to have a large surface area and more active sites for hydrogen catalytic performance.

Over the past few years, numerous efforts have focused on the synthesis of g-C₃N₄. Heating the carbon- and nitrogen-containing precursors was the primary method of producing graphite carbon nitride [16]. Cyanamide, cyanuric chloride, ethylenediamine with carbon tetrachloride, and melamine are among the most frequently utilized substances in synthesis [17]. Additionally, the usage of templates allows for the synthesis of materials with regular structures [18]. The ability to electrostatically self-assemble composite structures with negatively surface-charged materials to function because cocatalysts are one of the main benefits of the positively charged g-C₃N₄ material [19]. The surface of g-C₃N₄-TiO₂ was modified with phosphorous for hydrogen generation from NaBH₄ methanolysis [20]. The data showed a hydrogen evolution rate of 14,750 mL/g·min. Furthermore, the activation energy for hydrolysis was estimated to be 36.17 kJ mol⁻¹. Kottaikalai Ganesan et al. [21] reported utilizing phosphorylated silica (SP-PA) particles for the catalytic hydrolysis of sodium borohydride to produce hydrogen. In comparison to silica particles (133 mL min⁻¹g⁻¹ of catalyst), SP-PA particles generate hydrogen at a rate of 762.4 mL min⁻¹g⁻¹. The remarkable catalytic activity of SP-PA particles is indicated by the computed activation energy of 29.92 kJ mol⁻¹ for NaBH₄ hydrolysis. Fanghui Wang et al. [22] synthesized Co-P/CNTs-Ni foam for catalytic hydrogen generation at methanolysis of NaBH₄. The dandelion-like structure of the Co-P/CNTs-Ni foam catalysts was maintained and produced a maximum amount of hydrogen (2430 mL min⁻¹g⁻¹) at a temperature of 298 K. The data showed that NaBH₄ hydrolysis has an activation energy of 49.94 kJ mol⁻¹. Another study used calcination and hydrothermal techniques to generate a hybrid g-C₃N₄-SiO₂-N composite [23]. The experiments conducted using an NaBH₄ content of 0.25 g revealed a maximal hydrogen evolution rate of 11,400 mL min⁻¹g⁻¹. According to calculations, the hydrolysis of NaBH₄ has an activation energy of 33.2 kJ mol⁻¹. Cafer Saka [24] prepared catalysts of sulfur and nitrogen-doped metal-free microalgal carbon that are very active for the dehydrogenation of sodium borohydride in methanol. Their study achieved a maximal hydrogen generation rate of 26,000 mL min⁻¹g⁻¹. Meanwhile, the activation energy for hydrolysis was 10.59 kJ mol⁻¹. Highly dispersed CoB alloys implanted on MOF-74-derived graphene nanosheets were synthesized using the chemical reduction technique [25]. The catalytic hydrogen evolution measurements showed a value of 7937 mL min⁻¹g⁻¹ for the hydrolysis of NaBH₄. Furthermore, the investigation of activation energy for hydrolysis was evaluated as 38.8 kJ mol⁻¹.

Graphitic carbon nitride suffers from low conductivity and a small electroactive surface area. Low carrier mobility and excessive bulk recombination are the main reasons limiting the efficiency of g-C₃N₄. Therefore, researchers proposed many techniques to im-

prove conductivity and surface area by elemental doping, converting into nanosheets, and combining with metal nanoparticles and other carbon nanomaterials. This in turn will suppress the electron–hole recombination. The in situ polycondensation process can produce metal/g-C₃N₄ nanocomposites. Meanwhile, this synthesis procedure enables the direct formation of nanocomposites as well as microstructure control. Moreover, this technique has excellent aggregate elimination/reduction along with ideal and reproducible properties.

The current study aims to find an appropriate precursor, morphology, exfoliation condition, and fabrication processes for g-C₃N₄ in order to improve the catalytic activity. Furthermore, NiS nanostructures can be integrated in situ into the g-C₃N₄ nanosheet to increase the electroactive surface area and electrical conductivity. The in situ polycondensation process using different ratios of nickel chloride and thiourea at 550 °C for 120 min synthesized the NiS-g-C₃N₄ nanocomposite samples. The structural measurements for these nanocomposites was conducted using XRD, FTIR, and ESEM techniques. Moreover, an extensive study of the methanol hydrolysis of sodium borohydride was completed. Finally, the hydrogen catalytic efficiency of prepared materials was examined at methanolysis of NaBH₄. The hydrogen generation rates increased with increasing NiS nanosheet content. Moreover, the sample 1.5 wt.% NiS showed the highest production rate of 8654 mL/g·min.

2. Experimental

Loba Chemi, Mumbai, India supplied the chemicals (nickel chloride hexahydrate, thiourea, and sodium borohydride). The absolute methanol was provided by Sigma-Aldrich, Darmstadt, Germany. All provided chemicals were directly used without extra purification.

The bulk S@g-C₃N₄ was synthesized by heating 10.0 g of thiourea powder in a porcelain crucible covered with a lid in the muffle furnace at 550 °C (ramping rate = 3.0 °/min) and maintaining the temperature for 2 h. The yellow solid mass in a crucible was then allowed to cool to room temperature. Using an agate mortar, the resultant bulk S@g-C₃N₄ was crushed into a fine powder. The in situ polycondensation process using different ratios of nickel chloride and thiourea at 550 °C for 120 min synthesized NiS-g-C₃N₄ nanocomposite samples. In a typical synthesis, 10 g of thiourea powder and 0.5, 1.0 and 1.5 wt.% of nickel chloride were ground in an agate mortar for 30 min. After that, the powder was transferred to porcelain crucibles covered with a lid inserted inside a muffle furnace. The furnace operated at 550 °C for 120 min at a heating rate of 3.0 °C/min. The obtained nanocomposite samples were allowed to cool and then ground.

X-ray diffraction studies can analyze structural factors such as crystallinity, grain size, strain, phase composition, and structural defects. The XRD spectra were recorded from a Shimadzu XRD 700 instrument utilizing a Cu_{kα} wavelength of 1.54056 Å. Cu_{kα} radiation was created by using a Cu source as an X-ray source. The data scans were collected at the 2Theta range 5.0–80° with a count rate of 0.2°/min. The crystal structure was identified by comparing the diffraction pattern of the synthesized nanocomposite with the JCPDS files in the database. FTIR data were collected using a Shimadzu FTIR spectrometer—100 Tracer. The frequency ranges that can be examined are generally in the 4,000,399 cm^{−1} range. The sensitive characterization instrument ESEM exposes surface morphology and when coupled with an EDX (energy dispersive X-ray analysis) accessory, determines the elemental composition of materials. High-resolution 3D micrographs of the morphology were provided utilizing the ESEM technique. ESEM images and EDX data were acquired using a Thermo Fisher Quattro environmental scanning electron microscope (ESEM). Transmission electron microscopy (TEM) has become an essential tool in medical, biological, and materials' research because of its high magnifications. An investigation of TEM microscopy was carried out using a Thermo Fisher Scientific Talos F200i TEM/STEM electron microscope. The most generally used technique for calculating the specific surface area of produced material is the Brunauer–Emmett–Teller (BET) method. The BET technique involves the multi-layer adsorption of chemically inert N₂ gas with relative pressure and gas volume adsorbed in cm³/gm. The samples were degassed at 100 °C overnight to remove

trapped moisture molecules. The samples were subjected to N₂ gas at 77 K to record the adsorption–desorption isotherm on NOVA 4200e surface area analyzer. As a significant characterization tool in the field of photocatalysis, UV–Vis spectroscopy is a non-destructive method for analyzing optical characteristics such as absorbance, reflectance, transmittance, and bandgap energy that are related to the chemical composition of the material. In order to move electrons from their ground state to their excited state for electronic spectroscopy, it is necessary to absorb photons in the UV–visible region of the spectrum. The UV–Vis spectra were recorded on Agilent Cary 60 Spectrophotometer. The photoluminescence (PL) approach has been widely applied in the field of photocatalysis to study surface processes. Photoluminescence (PL) spectra at room temperature were obtained using a Cary Eclipse fluorescence spectrometer with a 350 nm excitation wavelength.

The hydrogen catalytic efficiency of prepared materials was evaluated as follows. Typically, 20 mg of the nanocomposite sample was mixed with 0.25 g of NaBH₄ and 10 mL of methanol was added without stirring. The hydrogen gas volume was recorded via the water displacement method. The measurements were completed at a temperature of 30 °C.

3. Results and Discussion

XRD is a non-destructive analytical method that provides details of the physical characteristics and crystalline structure of materials. The results of XRD data for the synthesized S@g-C₃N₄ and NiS-g-C₃N₄ nanocomposite catalysts are presented in Figure 1. The catalyst included a variety of compounds which were discovered using XRD analysis. The presence of two major peaks at 13.08° and 27.20° were observed in the spectrum of S@g-C₃N₄. The small diffraction peak at 13.08° matched a (100) plane with a distance of 0.676 nm [26,27]. The highest diffraction peak with reflection (002) was a typical interlayer stacking peak for graphitic C₃N₄ material and located at 2θ = 27.20°, which occurs because the atomic radius of sulfur is larger than carbon and nitrogen. Further, small diffraction peaks of sulfur were observed in the XRD spectrum of S@g-C₃N₄ [28]. For NiS-g-C₃N₄ at 0.5, 1.0, and 1.5 wt.%, the peak (002) moved to 27.55°, 27.66° and 27.64°, respectively. The positions of these reflections shifted to higher angles and thus lowered d-values with increase in NiS content. This indicates a structural contraction along the layer-stacking direction, presumably because of a more extended condensation of the carbon nitride chains [29]. Moreover, this shift occurs because of the reduced size (layer thickness) in carbon nitride sheets [30].

The reflections of NiS are located at 30.24°, 34.54°, 45.65°, 53.34°, 60.71°, and 62.94° that corresponds to (100), (101), (102), (110), (103), and (200) of hexagonal crystal structure (ICDD No. 50-1791). The synthesis of the NiS-g-C₃N₄ nanocomposites is confirmed by the existence of the two phases. Meanwhile, the crystallite size (*D*) is inversely proportional to the diffraction peak broadening (*β*) as proposed by the Scherer equation [31,32]:

$$D = \frac{0.9\lambda}{\beta \cos \theta} \quad (1)$$

Accordingly, the calculations of *b* at the diffraction peak with reflection (002) for S@g-C₃N₄ decreased as the NiS concentration increased from 0.5 to 1.5 wt.%. This reveals the small crystallite domains of S@g-C₃N₄. The calculation of NiS crystallites reveals an average size of 8.0 nm for 0.5 wt.% NiS, 1.0 wt.% NiS, and 1.5 wt.% NiS. Moreover, the shift of peak position for the (002) plane after the growth of NiS at different content (0.0–1.5 wt.%) confirms the successful formation of nanocomposites.

Figure 2 shows the FTIR spectra of S@g-C₃N₄ and NiS-g-C₃N₄ nanocomposite samples. The vibrations of C–O stretching and C–OH stretching for the S@g-C₃N₄ sample located at 1010 and 1132 cm^{−1} [33]. This result indicates the existence of both hydroxyl (C–OH), carbonyl (C=O), and carboxylic (COOH). The vibrations of N–H stretching or the H₂O adsorption showed two peaks at 3100–3300 cm^{−1} [34]. The absorption bands between 1229 and 1628 cm^{−1} observed in the spectrum of S@g-C₃N₄ correspond to the typical stretching modes of CN heterocycles [35]. It was determined that the physically adsorptive CO₂ from

the environment was responsible for a weak band at 2336 cm^{-1} [30]. Moreover, another weak peak connected to the C=N bond was seen at 2170 cm^{-1} [36].

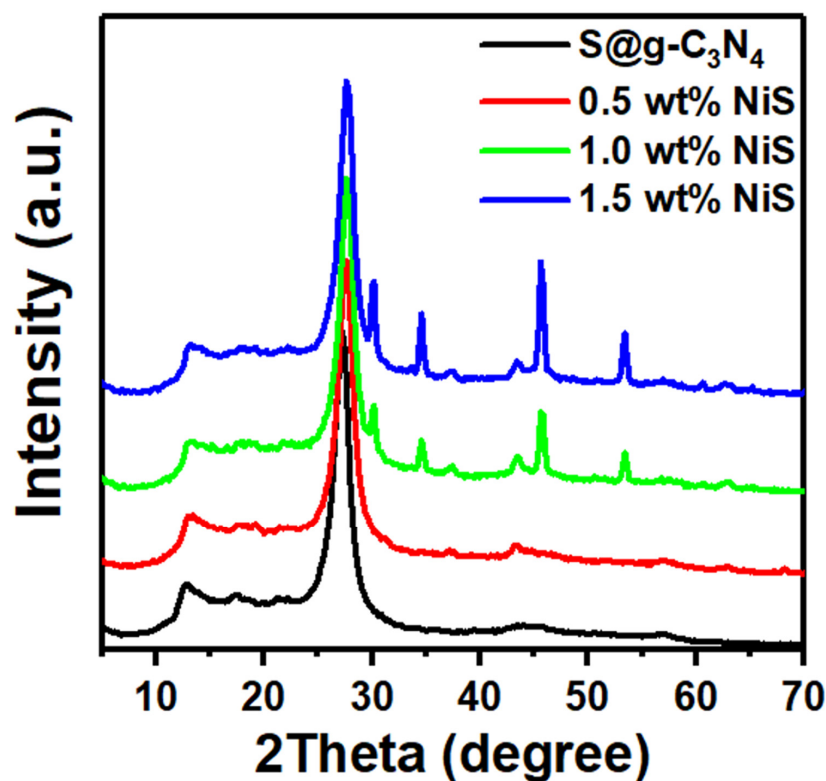


Figure 1. XRD data of S@g-C₃N₄ and NiS-g-C₃N₄ nanocomposites.

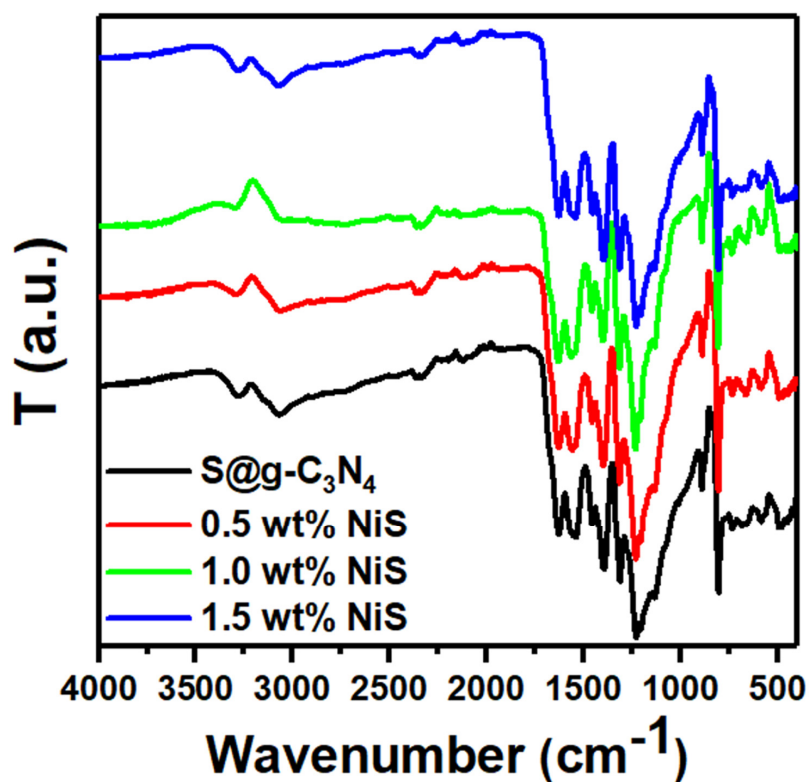


Figure 2. FTIR data of S@g-C₃N₄ and NiS-g-C₃N₄ nanocomposites.

The medium intense sharp band at around 804 cm^{-1} suggests the samples consist of triazine or heptazine building blocks [37]. The bands at 1205 and 1311 cm^{-1} indicate the presence of C–N (sp^3) and C–N(–C)–C bonds [38]. Moreover, the positions of these peaks slightly shift to a higher wavenumber after the growth of NiS at 1.5 wt.%. These outcomes provide evidence of the successful preparation of NiS-g-C₃N₄ nanocomposites and agree with the XRD investigations.

The morphology and structure of the synthesized S@g-C₃N₄ and NiS-g-C₃N₄ nanocomposite samples were investigated by ESEM images. In Figure 3, S@g-C₃N₄ shows that a 2D sheet structure was achieved for g-C₃N₄ materials. NiS-g-C₃N₄ nanocomposites showed the sheet materials were broken up during the growth process in Figure 3, revealing more edge sites. This aligns with the XRD result showing that NiS-g-C₃N₄ is less ordered and crystalline by virtue of the broader spectral peaks.

The EDX spectra displayed in Figure S1 (Supplementary Materials) of the NiS-g-C₃N₄ nanocomposite samples confirm the presence of all the elements supposed. Table 1 also displays the weight percent of the elements found on the samples' surfaces. Moreover, Figure S1 shows no identifiable peaks for any other elements besides Ni, S, C, and N, demonstrating that the NiS-g-C₃N₄ nanocomposite samples are of high purity.

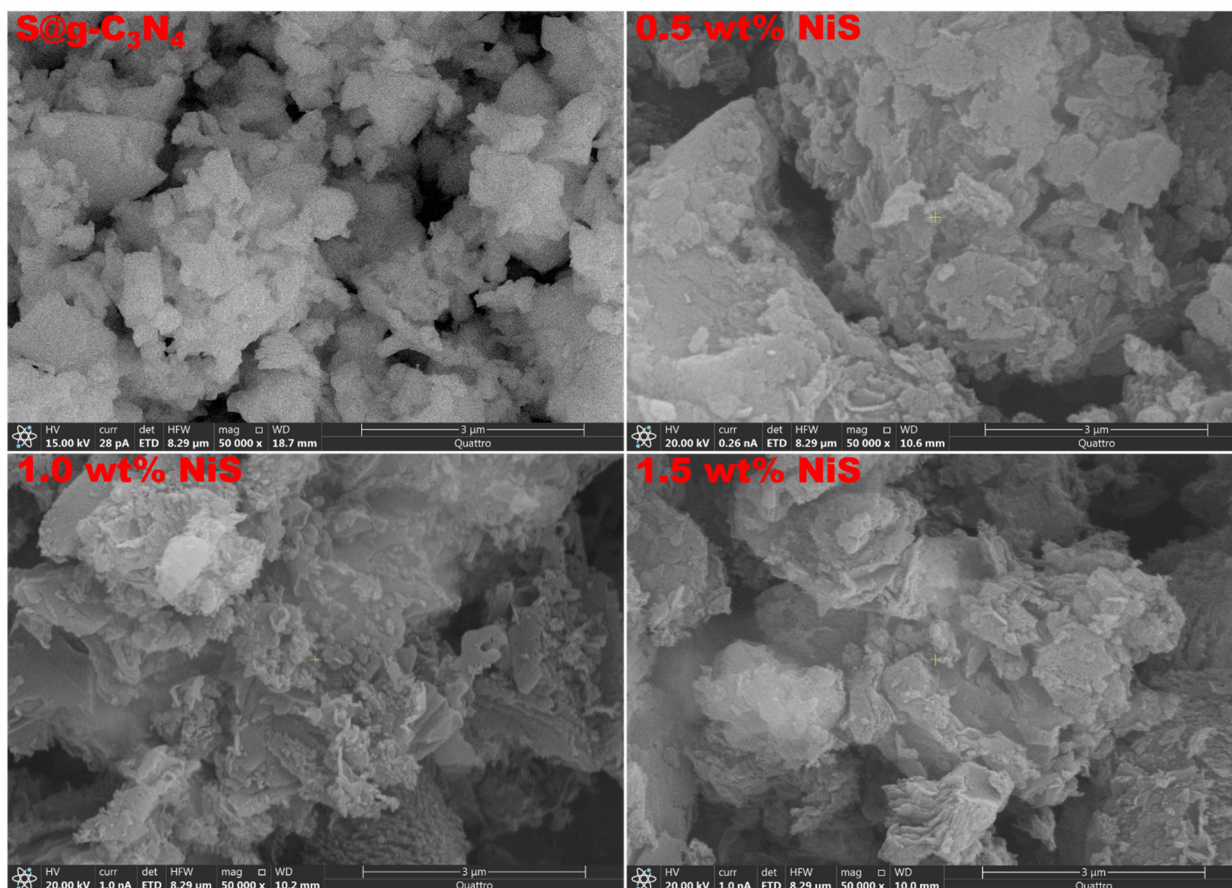


Figure 3. ESEM micrographs of S@g-C₃N₄ and NiS-g-C₃N₄ nanocomposites.

Table 1. Weight % of elements present at the surface of the NiS-g-C₃N₄ samples analyzed from EDX analysis.

Sample	C (wt.%)	N (wt.%)	S (wt.%)	Ni (wt.%)
0.5 wt.% NiS	37.75	61.14	0.17	0.94
1.0 wt.% NiS	46.11	52.13	0.30	1.47
1.5 wt.% NiS	35.64	57.27	1.08	6.01

TEM images of S@g-C₃N₄ and 1.5 wt.% NiS nanocomposite samples are shown in Figure 4. The lamellar structure with sheet morphology is seen in the images. The image of S@g-C₃N₄ reveals stack layers that are connected with XRD and ESEM measurements. Moreover, the sheet materials in 1.5 wt.% NiS nanocomposite sample were broken up throughout the growing process.

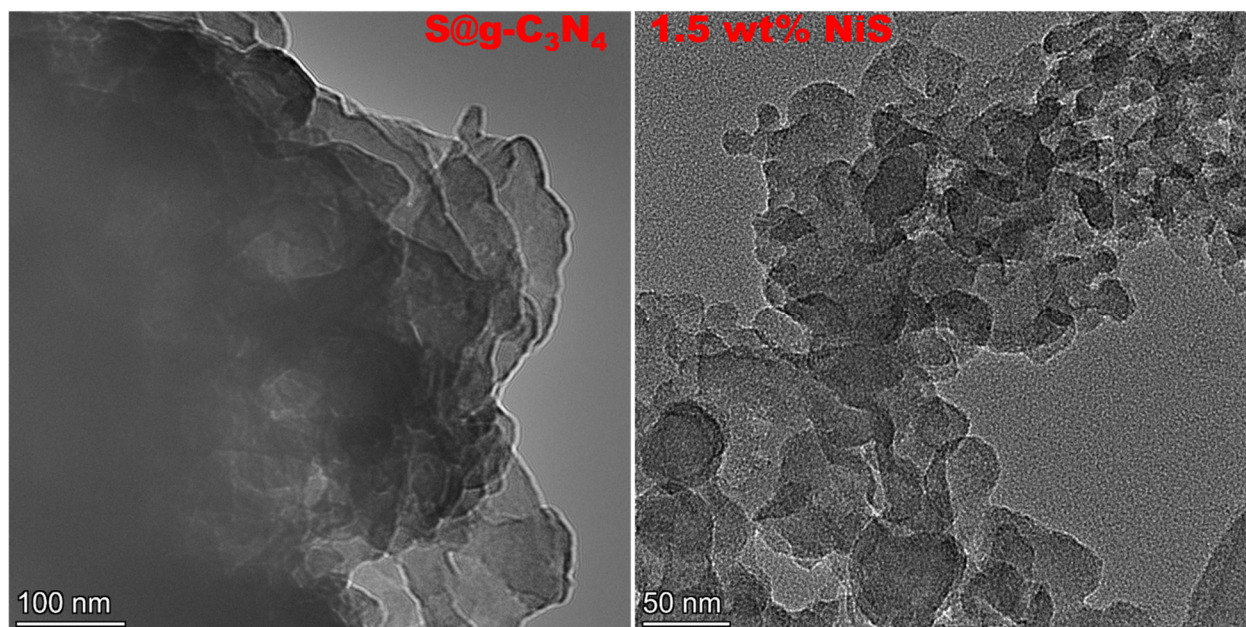


Figure 4. TEM micrographs of S@g-C₃N₄ and 1.5 wt.% NiS nanocomposites.

An adsorbent surface area, which is directly related to the number of active sites for adsorption, has a significant impact on its catalytic activity. We measured surface area using the N₂ adsorption–desorption isotherm at 77 K for the S@g-C₃N₄ and NiS-g-C₃N₄ nanocomposite samples (Figure 5). All the samples exhibited type IV isotherm with no saturation implying mesoporous nature. BET plots give specific surface areas of 40, 65, 66, and 83 m²/g for S@g-C₃N₄, 0.5 wt.% NiS, 1.0 wt.% NiS, and 1.5 wt.% NiS, respectively. The surface area represents the effect of the in situ polycondensation preparation of S@g-C₃N₄ and NiS-g-C₃N₄ nanocomposites. The BJH pore volume of S@g-C₃N₄ is 0.18 cm³, which increases to 0.20 cm³ in 1.5 wt.% NiS owing to the incorporation of NiS into the nanosheet. We found that the in situ polycondensation preparation of S@g-C₃N₄ and NiS-g-C₃N₄ nanocomposites increased the porosity of the composites, which allowed for more interaction with ions and faster electron transport for catalytic activity [39].

The absorbance properties of S@g-C₃N₄ and NiS-g-C₃N₄ nanocomposite samples were measured with the help of UV–visible spectroscopy as shown in Figure 6a. The absorbance curve displays a significant absorption band centered around 322 nm that corresponds to n→π* electronic transitions. Heterocyclic aromatics showed the band gap absorption around 400 nm that corresponds to the characteristic π-π* transitions [8]. It is also expected that the disorder in nanocomposites will result in separated electron and hole states with energies in the band gap, causing the Urbach tail in the optical absorption spectrum, which broadens the absorption even more. Moreover, a shoulder appeared at 400 nm that showed a red shift when NiS content varies from 0.0–1.5 wt.%. The red shift in adsorption revealed the ease of production of photo-induced electrons and holes.

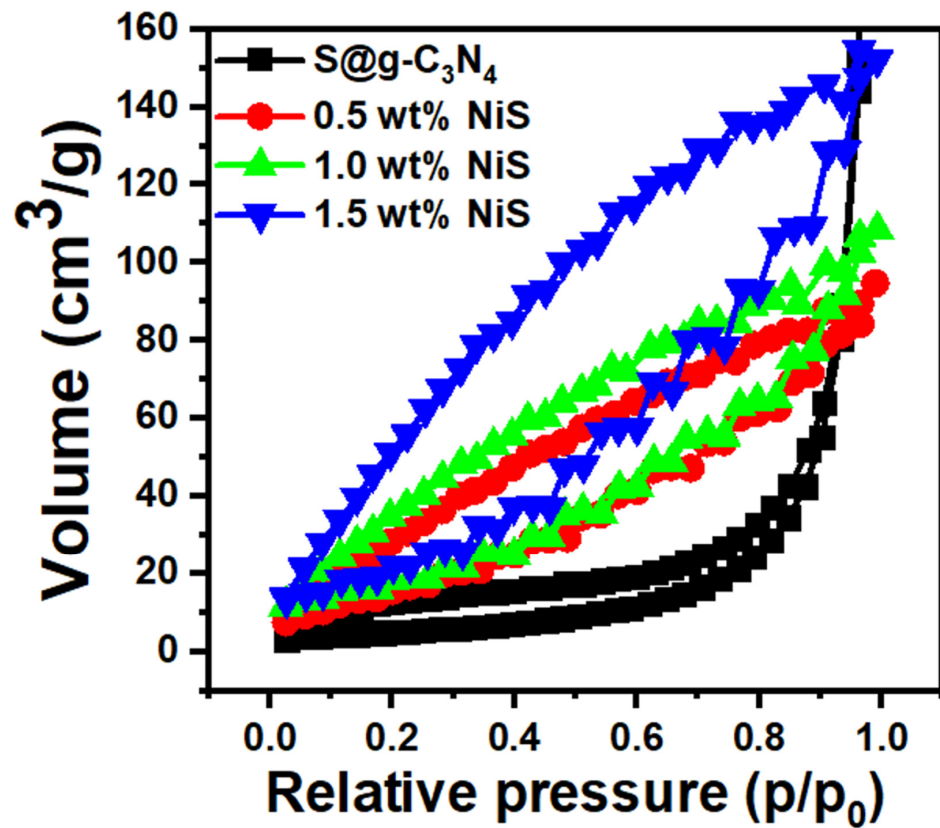


Figure 5. Nitrogen adsorption–desorption isotherm of S@g-C₃N₄ and NiS-g-C₃N₄ nanocomposites.

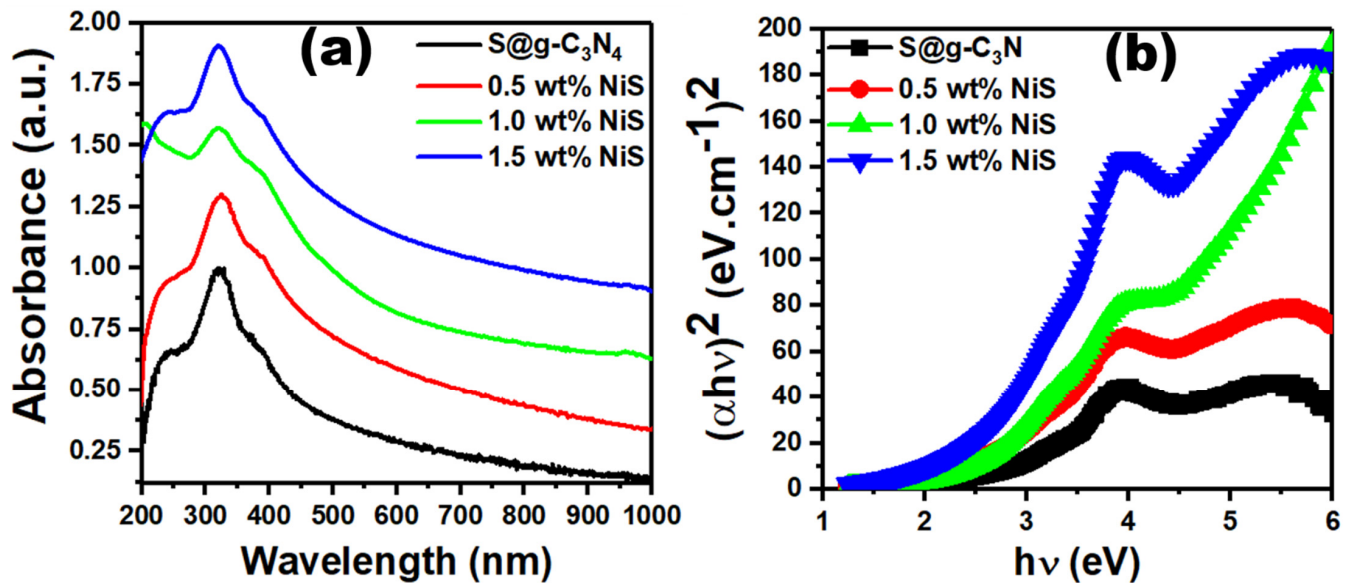


Figure 6. Graphs of (a) absorbance vs. wavelength and (b) $(\alpha h\nu)^2$ vs. photon energy for S@g-C₃N₄ and NiS-g-C₃N₄ nanocomposites.

The optical energy gap (E_{opt}) is an important parameter to estimate the electronic structure of the S@g-C₃N₄ and NiS-g-C₃N₄ nanocomposites. E_{opt} is calculated by evaluation of the straight lines intercept at zero photon absorption from the plots of $(\alpha h\nu)^2$ vs. photon energy ($h\nu$) shown in Figure 6b as follows [40–42]:

$$\alpha h\nu = k(h\nu - E_g)^{0.5} \quad (2)$$

The average values of the optical energy gap for S@g-C₃N₄ were 2.60 eV that decreased to 2.50, 2.40, and 2.30 eV as the NiS concentration increased from 0.5 to 1.5 wt.%. This decrease in the energy gap is explained by the development of additional energy levels or changes in the g-C₃N₄ electronic structure [43,44].

Physical and chemical characteristics of materials are measured in photoluminescence by employing photons to produce excited electronic states in the material system and evaluating the optical emission when these states relax. This in turn induces electron-hole pairs that recombine after a lifetime in excited states. The key factors influencing a catalyst's capacity to catalyze a reaction are the electrical and structural defects as well as the recombination of electron-hole pairs [45]. Figure 7 shows the emission spectra of S@g-C₃N₄ and NiS-g-C₃N₄ nanocomposites. All NiS-g-C₃N₄ nanocomposite catalysts have an emission band that is visible in the 410–540 nm range and is composed of n- π^* transitions [46]. The intensity of this peak decreased as the NiS concentration increased from 0.5 to 1.5 wt.%. This could be because electron-hole pairs are produced quickly while the pair recombination process is delayed. Further, the photo-induced electron-hole pair can transfer easily at the interface of NiS/g-C₃N₄ nanocomposite. As a result, we expect that the nanocomposite sample 1.5 wt.% NiS will show high catalytic performance concerning the other samples.

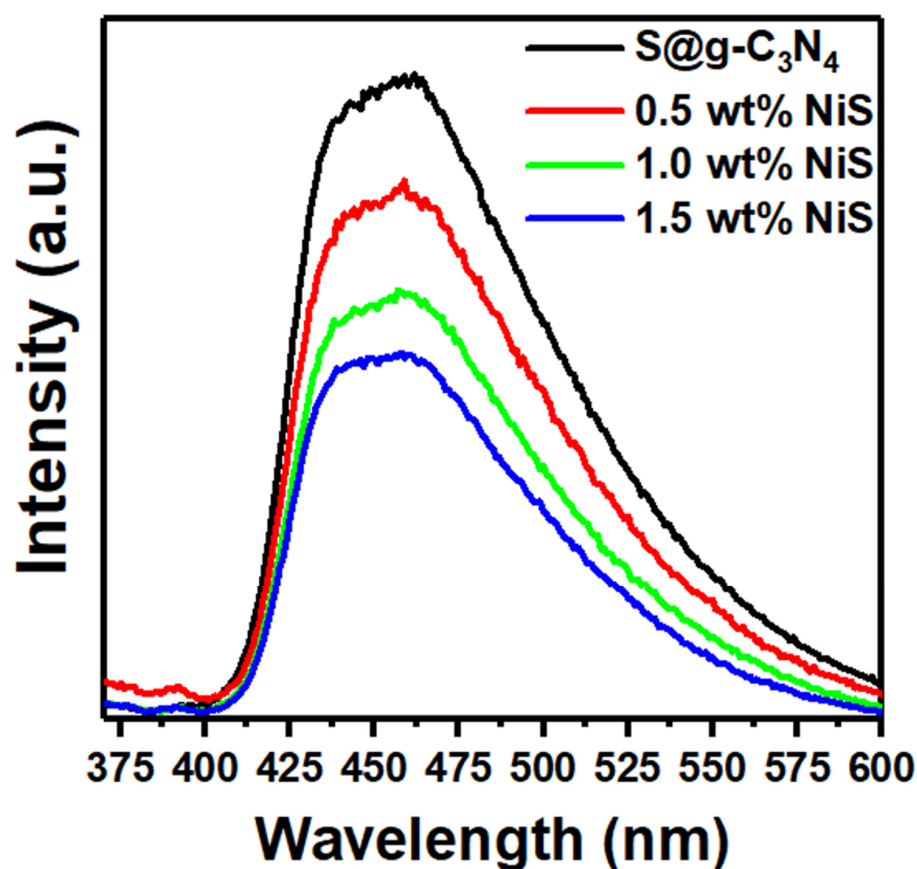


Figure 7. PL spectra for S@g-C₃N₄ and NiS-g-C₃N₄ nanocomposites.

In self-hydrolysis, sodium borohydride solutions become chemically stable and do not produce substantial quantities of H₂ at ambient conditions. In pure water, sodium borohydride undergoes self-hydrolysis, consuming H₃O⁺ ions, and causing a pH rise that lowers the rate at which hydrogen is produced [47]. Methanol is one of the highest reactivity reagents toward sodium borohydride and is the lightest alcohol, which makes it a suitable alternative for water in the reaction that produces hydrogen. Another benefit of employing methanol is that it lowers the reactant mixture's freezing point, making

it feasible to generate hydrogen at temperatures lower than 273 K with rapid hydrogen synthesis and quick reaction initiation—impossible when using pure water. Moreover, methanol regeneration may be employed as a possible high gravimetric density hydrogen storage device, and sodium borohydride methanolysis has been presented as a practical process for hydrogen production at low temperatures [48].

According to the Langmuir–Hinshelwood mechanism, catalysts whose surfaces are linked with the amino group effectively contribute to the hydrolysis or methanolysis of NaBH_4 and for hydrogen generation. Meanwhile, methanol and NaBH_4 molecules adsorb on the catalyst's surface [49,50]. On the other hand, Michaelis–Menten stated that the active sites of the catalyst adsorb NaBH_4 without methanol [51,52]. The aforementioned information leads to the conclusion that catalyst surface characteristics are crucial for the evolution of hydrogen gas.

Nanocomposite catalysts are employed to accelerate the kinetics of sodium borohydride hydrolysis in stable solutions, resulting in a significant increase in hydrogen production. The particle size and degree of dispersion are other factors that affect a catalyst's activity. In order to speed up the reaction and lower the catalyst loading, small particle size and excellent dispersion encourage extensive catalyst interaction with the NaBH_4 solution. A methanolysis experiment was performed in order to check the role of $\text{S@g-C}_3\text{N}_4$ and $\text{NiS-g-C}_3\text{N}_4$ nanocomposites in the hydrogen evolution from NaBH_4 . The data were recorded at 30 °C and plotted in Figure 8. $\text{S@g-C}_3\text{N}_4$ and $\text{NiS-g-C}_3\text{N}_4$ nanocomposites were added and led to an increase in the maximum quantity of hydrogen. The sample 1.5 wt.% NiS showed the fastest hydrogen generation performance. In methanol, the NaBH_4 material broke down into Na^+ and BH_4^- ions. Moreover, the surface of $\text{S@g-C}_3\text{N}_4$ and $\text{NiS-g-C}_3\text{N}_4$ nanocomposites adsorbed BH_4^- ions. The efficient catalyst adsorbs more BH_4^- ions in a short time and thus produces more hydrogen.

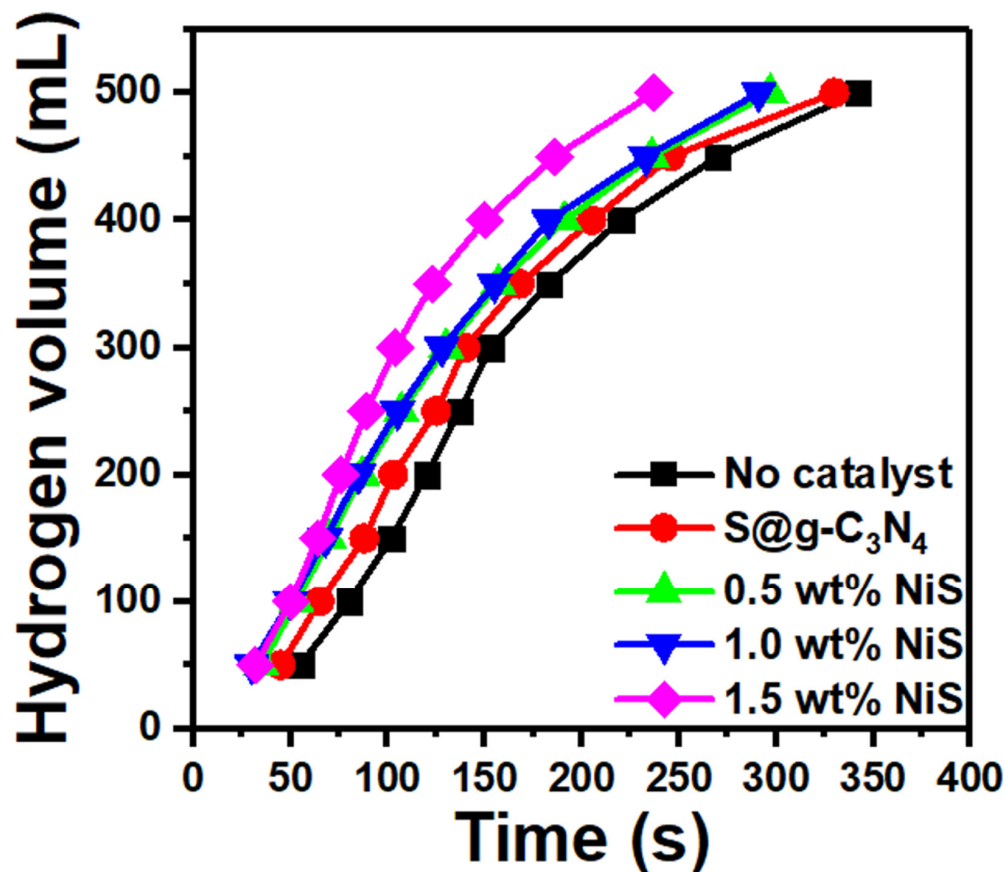


Figure 8. Hydrogen production from methanolysis of NaBH_4 of $\text{S@g-C}_3\text{N}_4$ and $\text{NiS-g-C}_3\text{N}_4$ nanocomposites.

The rate of hydrogen production greatly determines the efficiency of the catalyst to speed up the reaction. Hydrogen evolution rates (r) of the S@g-C₃N₄ and NiS-g-C₃N₄ nanocomposites are calculated with help of the following equations using the H₂ volume (V), the mass of catalyst (m_{cat}), and time of reaction (t) [20,53]:

$$r = \frac{V}{t \cdot m_{cat}} \quad (3)$$

The hydrogen evolution curves displayed in Figure 8 were used to calculate the hydrogen generation rate. The calculated production rates are plotted in Figure 9 for the S@g-C₃N₄ and NiS-g-C₃N₄ samples. The hydrogen generation rates increased with the increase in the NiS nanosheet content. Moreover, the sample 1.5 wt.% NiS showed the highest production rate of 8654 mL/g·min. The nanocomposite 1.5 wt.% NiS had the highest generation rate among others due to the promising surface design [54]. In this context, NaBH₄ decomposes in methanol into Na⁺ and BH₄⁻ ions. The large surface area of the nanocomposite sample 1.5 wt.% NiS helps the adsorption of more BH₄⁻ ions. As a result, the production of hydrogen from methanolysis of NaBH₄ will be accelerated. Additionally, this rate of hydrogen evolution (8654 mL/g·min) exceeds the rates for R-TiO₂-NH₂ (3525 mL/g·min) [50], SiO₂@PAA (5120 mL/g·min) [55], ZIF-67@GO (3200 mL/g·min) [56], and Ru/NiO-Ni foam (6000 mL/g·min) [57].

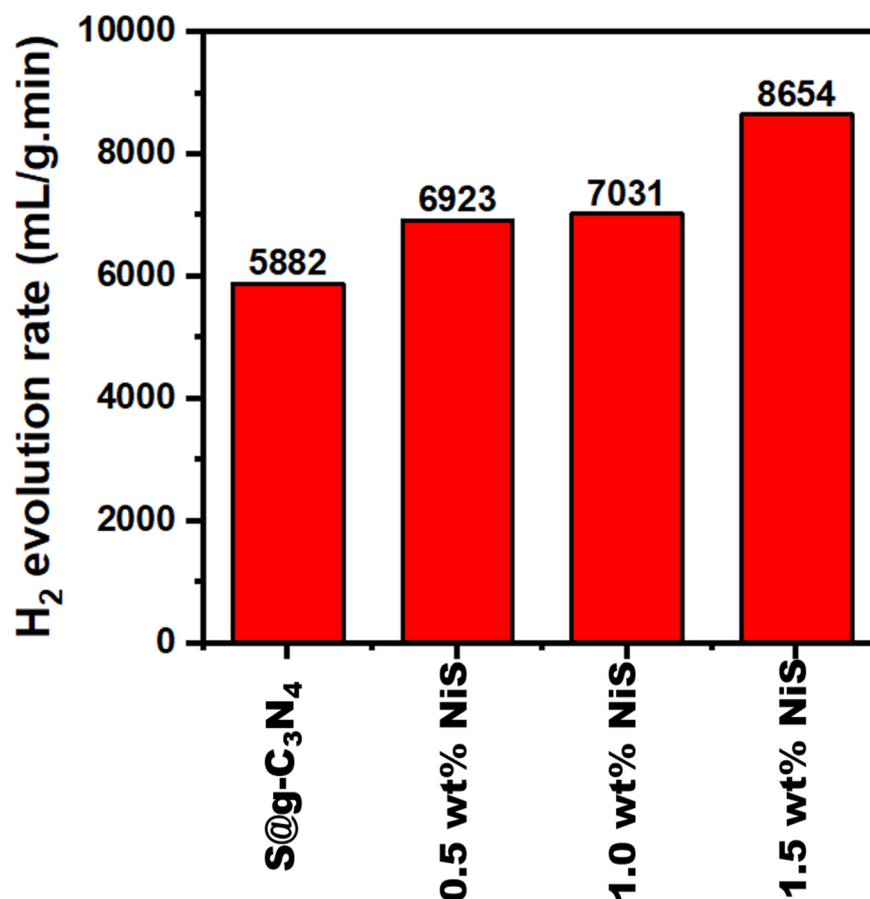


Figure 9. H₂ production rates for S@g-C₃N₄ and NiS-g-C₃N₄ nanocomposites.

4. Conclusions

The in situ polycondensation method was implemented for the preparation of S@g-C₃N₄ and NiS-g-C₃N₄ and was employed for catalytic hydrogen production from the methanolysis of sodium borohydride. The incorporation of NiS during the growth process played a major role in the enhancement of the surface area and porosity of the S@g-C₃N₄

composites. The 1.5 wt.% NiS sample had the highest surface area of $90 \text{ m}^2/\text{g}$ compared with the 0.5 wt.% NiS and 1.0 wt.% NiS samples. The pore volume of S@g-C₃N₄ was 0.18 cm^3 , which was reduced to 0.11 cm^3 in 1.5 wt.% NiS owing to the incorporation of NiS particles into the nanosheet. We found that during the in situ polycondensation preparation of S@g-C₃N₄ and NiS-g-C₃N₄ nanocomposites increased the porosity of the composites. The average value of the optical energy gap for S@g-C₃N₄ was 2.60 eV and decreased to 2.30 eV because of the 1.5 wt.% NiS incorporation. The NiS-g-C₃N₄ catalysts showed an emission band in the 410–540 nm range and the intensity of this peak decreased as the NiS concentration increased from 0.5 to 1.5 wt.%. The hydrogen generation rates increased with the increase in the NiS nanosheet content. The sample 1.5 wt.% NiS showed the highest production rate of 8654 mL/g·min compared with others due to the promising surface design. The large surface area of the nanocomposite sample 1.5 wt.% NiS helps for adsorption of more BH₄[−] ions. As a result, the production of hydrogen from methanolysis of NaBH₄ will be accelerated. All of these results enhance the possibility of using 1.5 wt.% NiS as a promising catalyst for the production of hydrogen from NaBH₄ methanolysis.

Supplementary Materials: The following supporting information can be downloaded at: <https://www.mdpi.com/article/10.3390/nano13050938/s1>, Figure S1: EDX data for NiS-g-C₃N₄ nanocomposites.

Author Contributions: Conceptualization, A.H.A. and T.A.M.T.; validation, T.A.M.T., S.A., T.A.; formal analysis, M.A. and K.A.; resources, A.H.A.; writing—original draft preparation, M.A, K.A., S.A. and T.A.; writing—review and editing, A.H.A. and T.A.M.T.; supervision and funding acquisition, A.H.A. All authors have read and agreed to the published version of the manuscript.

Funding: The authors extend their appreciation to the Deputyship for Research and Innovation, the Ministry of Education in Saudi Arabia for funding this research work through the project number 223202.

Data Availability Statement: The corresponding author will make the data available on request.

Acknowledgments: The Authors thanks the central lab. At Jouf University for the advance techniques which have been used in this manuscript.

Conflicts of Interest: The authors declare no conflict of interest.

References

1. Wang, J.; Wang, S. A critical review on graphitic carbon nitride (g-C₃N₄)-based materials: Preparation, modification and environmental application. *Co-Ord. Chem. Rev.* **2022**, *453*, 214338. [CrossRef]
2. Bharagav, U.; Reddy, N.R.; Rao, V.N.K.; Ravi, P.; Sathish, M.; Rangappa, D.; Prathap, K.; Chakra, C.S.; Shankar, M.V.; Appels, L.; et al. Bifunctional g-C₃N₄/carbon nanotubes/WO₃ ternary nanohybrids for photocatalytic energy and environmental applications. *Chemosphere* **2023**, *311*, 137030. [CrossRef]
3. Rono, N.; Kibet, J.K.; Martincigh, B.S.; Nyamori, V.O. A review of the current status of graphitic carbon nitride. *Crit. Rev. Solid State Mater. Sci.* **2021**, *46*, 189–217. [CrossRef]
4. Hayat, A.; Al-Sehemi, A.G.; El-Nasser, K.S.; Taha, T.; Al-Ghamdi, A.A.; Syed, J.A.S.; Amin, M.A.; Ali, T.; Bashir, T.; Palamanit, A.; et al. Graphitic carbon nitride (g-C₃N₄)-based semiconductor as a beneficial candidate in photocatalysis diversity. *Int. J. Hydrogen Energy* **2021**, *47*, 5142–5191. [CrossRef]
5. Hayat, A.; Sohail, M.; Anwar, U.; Taha, T.A.; Qazi, H.I.A.; Ajmal, Z.; Abdullah, G.A.S.; Hamed, A.; Ahmed, A.A.G.; Mohammed, A.A.; et al. A Targeted Review of Current Progress, Challenges and Future Perspective of g-C₃N₄ based Hybrid Photocatalyst Toward Multidimensional Applications. *Chem. Rec.* **2022**, *23*, e202200143.
6. Hao, Q.; Jia, G.; Wei, W.; Vinu, A.; Wang, Y.; Arandiyani, H.; Ni, B.-J. Graphitic carbon nitride with different dimensionalities for energy and environmental applications. *Nano Res.* **2020**, *13*, 18–37. [CrossRef]
7. Liu, J.; Wang, H.; Antonietti, M. Graphitic carbon nitride “reloaded”: Emerging applications beyond (photo) catalysis. *Chem. Soc. Rev.* **2016**, *45*, 2308–2326. [CrossRef]
8. Wang, A.-J.; Li, H.; Huang, H.; Qian, Z.-S.; Feng, J.-J. Fluorescent graphene-like carbon nitrides: Synthesis, properties and applications. *J. Mater. Chem. C* **2016**, *4*, 8146–8160. [CrossRef]
9. Harun, N.A.M.; Shaari, N.; Ramli, Z.A.C. Progress of g-C₃N₄ and carbon-based material composite in fuel cell application. *Int. J. Energy Res.* **2022**, *46*, 16281–16315. [CrossRef]
10. El-Sayed, S.A. Review of thermal decomposition, kinetics parameters and evolved gases during pyrolysis of energetic materials using different techniques. *J. Anal. Appl. Pyrolysis* **2022**, *161*, 105364. [CrossRef]

11. Muniyappa, M.; Kalegowda, S.N.; Shetty, M.; Sriramoju, J.B.; Shastri, M.; Nabakoteswara Rap, S.V.; Debasis, D.; Shankar, M.V.; Rangappa, D. Cocatalyst free nickel sulphide nanostructure for enhanced photocatalytic hydrogen evolution. *Int. J. Hydrogen Energy* **2022**, *47*, 5307–5318. [[CrossRef](#)]
12. NavakoteswaraRao, V.; Shankar, M.V.; Yang, B.L.; Ahn, C.W.; Yang, J.M. Effective excitons separation in starfish Bi₂S₃/TiO₂ nanostructures for enhanced hydrogen production. *Mater. Today Chem.* **2022**, *26*, 101096. [[CrossRef](#)]
13. He, K.; Xie, J.; Li, M.; Li, X. In situ one-pot fabrication of g-C₃N₄ nanosheets/NiS cocatalyst heterojunction with intimate interfaces for efficient visible light photocatalytic H₂ generation. *Appl. Surf. Sci.* **2018**, *430*, 208–217. [[CrossRef](#)]
14. Wen, J.; Xie, J.; Zhang, H.; Zhang, A.; Liu, Y.; Chen, X.; Li, X. Constructing Multifunctional Metallic Ni Interface Layers in the g-C₃N₄ Nanosheets/Amorphous NiS Heterojunctions for Efficient Photocatalytic H₂ Generation. *ACS Appl. Mater. Interfaces* **2017**, *9*, 14031–14042. [[CrossRef](#)] [[PubMed](#)]
15. Wang, M.; Cheng, J.; Wang, X.; Hong, X.; Fan, J.; Yu, H. Sulfur-mediated photodeposition synthesis of NiS cocatalyst for boosting H₂-evolution performance of g-C₃N₄ photocatalyst. *Chin. J. Catal.* **2021**, *42*, 37–45. [[CrossRef](#)]
16. Liu, J.; Fu, W.; Liao, Y.; Fan, J.; Xiang, Q. Recent advances in crystalline carbon nitride for photocatalysis. *J. Mater. Sci. Technol.* **2021**, *91*, 224–240. [[CrossRef](#)]
17. Fronczak, M. Adsorption performance of graphitic carbon nitride-based materials: Current state of the art. *J. Environ. Chem. Eng.* **2020**, *8*, 104411. [[CrossRef](#)]
18. Shcherban, N.; Shvalagin, V.; Korzhak, G.; Yaremov, P.; Skoryk, M.; Sergiienko, S.; Kuchmiy, S.Y. Hard template synthesis and photocatalytic activity of graphitic carbon nitride in the hydrogen evolution reaction using organic acids as electron donors. *J. Mol. Struct.* **2021**, *1250*, 131741. [[CrossRef](#)]
19. Guru, S.; Kumar, S.; Bellamkonda, S.; Gangavarapu, R.R. Synthesis of CuTi-LDH supported on g-C₃N₄ for electrochemical and photoelectrochemical oxygen evolution reactions. *Int. J. Hydrogen Energy* **2021**, *46*, 16414–16430. [[CrossRef](#)]
20. Saka, C. Phosphorus decorated g-C₃N₄-TiO₂ particles as efficient metal-free catalysts for hydrogen release by NaBH₄ methanolysis. *Fuel* **2022**, *322*, 124196. [[CrossRef](#)]
21. Ganesan, K.; Hayagreevan, C.; Rahul, R.; Jeevagan, A.J.; Adinaveen, T.; Bhuvaneshwari, D.S.; Muthukumar, P.; Amalraj, M. Catalytic hydrolysis of sodium borohydride for hydrogen production using phosphorylated silica particles. *Environ. Sci. Pollut. Res.* **2022**, *30*, 21199–21212. [[CrossRef](#)] [[PubMed](#)]
22. Wang, F.; Zhang, Y.; Luo, Y.; Wang, Y.; Zhu, H. Preparation of dandelion-like Co–Mo–P/CNTs–Ni foam catalyst and its performance in hydrogen production by alcoholysis of sodium borohydride. *Int. J. Hydrogen Energy* **2020**, *45*, 30443–30454. [[CrossRef](#)]
23. Saka, C. Efficient and durable H₂ production from NaBH₄ methanolysis using N doped hybrid g-C₃N₄-SiO₂ composites with ammonia as a nitrogen source. *Fuel* **2022**, *324*, 124594. [[CrossRef](#)]
24. Saka, C. Sulphur and nitrogen-doped metal-free microalgal carbon catalysts for very active dehydrogenation of sodium borohydride in methanol. *Int. J. Hydrogen Energy* **2021**, *46*, 18326–18337. [[CrossRef](#)]
25. Zhang, H.; Wei, Q.; Wu, G.; Qiu, S.; Zou, Y.; Xia, Y.; Xu, F.; Sun, L.; Chu, H. Zn-MOF-74-derived graphene nanosheets supporting CoB alloys for promoting hydrolytic dehydrogenation of sodium borohydride. *J. Alloys Compd.* **2023**, *930*, 167486. [[CrossRef](#)]
26. Xue, X.; Zhang, J.; Li, M.; Ao, C.; Wang, Q.; Zhao, J.; Zhang, W.; Lu, C. Facile fabrication of three-dimensional nanofibrous foams of cellulose@g-C₃N₄@Cu₂O with superior visible-light photocatalytic performance. *Carbohydr. Polym.* **2023**, *303*, 120455. [[CrossRef](#)]
27. Wang, Z.; Huo, Y.; Fan, Y.; Wu, R.; Wu, H.; Wang, F.; Xu, X. Facile synthesis of carbon-rich g-C₃N₄ by copolymerization of urea and tetracyanoethylene for photocatalytic degradation of Orange II. *J. Photochem. Photobiol. A Chem.* **2018**, *358*, 61–69. [[CrossRef](#)]
28. Chang, F.; Yan, W.; Cheng, W.; Wu, F.; Deng, B.; Hu, X. The construction and enhanced photocatalytic performance of binary composite S/g-C₃N₄. *Mater. Sci. Semicond. Process.* **2018**, *87*, 1–6. [[CrossRef](#)]
29. Thomas, A.; Fischer, A.; Goettmann, F.; Antonietti, M.; Müller, J.-O.; Schlögl, R.; Carlsson, J.M. Graphitic carbon nitride materials: Variation of structure and morphology and their use as metal-free catalysts. *J. Mater. Chem.* **2008**, *18*, 4893–4908. [[CrossRef](#)]
30. Vu, M.H.; Sakar, M.; Nguyen, C.C.; Do, T.O. Chemically bonded Ni cocatalyst onto the S doped g-C₃N₄ nanosheets and their synergistic enhancement in H₂ production under sunlight irradiation. *ACS Sustain. Chem. Eng.* **2018**, *6*, 4194–4203. [[CrossRef](#)]
31. Taha, T.A.; Saad, R.; Zayed, M.; Shaban, M.; Ahmed, A.M. Tuning the surface morphologies of ZnO nanofilms for enhanced sensitivity and selectivity of CO₂ gas sensor. *Appl. Phys. A* **2023**, *129*, 115. [[CrossRef](#)]
32. Manzoor, S.; Abid, A.G.; Aman, S.; Abdullah, M.; Rashid, A.R.; Ali, H.M.; Ali, T.E.; Assiri, M.A.; Ashiq, M.N.; Taha, T. Facile synthesis of CoFePO₄ on eggshell membrane for oxygen evolution reaction and supercapacitor applications. *Ceram. Int.* **2022**, *48*, 36975–36982. [[CrossRef](#)]
33. Fan, C.; Miao, J.; Xu, G.; Liu, J.; Lv, J.; Wu, Y. Graphitic carbon nitride nanosheets obtained by liquid stripping as efficient photocatalysts under visible light. *RSC Adv.* **2017**, *7*, 37185–37193. [[CrossRef](#)]
34. Lu, Q.; Deng, J.; Hou, Y.; Wang, H.; Li, H.; Zhang, Y. One-step electrochemical synthesis of ultrathin graphitic carbon nitride nanosheets and their application to the detection of uric acid. *Chem. Commun.* **2015**, *51*, 12251–12253. [[CrossRef](#)]
35. Gao, J.; Wang, J.; Qian, X.; Dong, Y.; Xu, H.; Song, R.; Yan, C.; Zhu, H.; Zhong, Q.; Qian, G.; et al. One-pot synthesis of copper-doped graphitic carbon nitride nanosheet by heating Cu–melamine supramolecular network and its enhanced visible-light-driven photocatalysis. *J. Solid State Chem.* **2015**, *228*, 60–64. [[CrossRef](#)]
36. Wang, Z.-T.; Xu, J.-L.; Zhou, H.; Zhang, X. Facile synthesis of Zn(II)-doped g-C₃N₄ and their enhanced photocatalytic activity under visible light irradiation. *Rare Met.* **2019**, *38*, 459–467. [[CrossRef](#)]

37. Bojdys, M.J.; Müller, J.-O.; Antonietti, M.; Thomas, A. Ionothermal Synthesis of Crystalline, Condensed, Graphitic Carbon Nitride. *Chem A Eur. J.* **2008**, *14*, 8177–8182. [[CrossRef](#)] [[PubMed](#)]
38. Xia, P.; Zhu, B.; Yu, J.; Cao, S.; Jaroniec, M. Ultra-thin nanosheet assemblies of graphitic carbon nitride for enhanced photocatalytic CO₂ reduction. *J. Mater. Chem. A* **2017**, *5*, 3230–3238. [[CrossRef](#)]
39. Vijayakumar, E.; Preetha, R.; Narendran, M.G.; Jennifer, G.A.; Varathan, E.; Neppolian, B.; Ganesh, V.K.; Bosco, A.J. Experimental investigation into the π -conjugated HT-g-C₃N₄/MoS₂ (X) evokes the electron transport in type-II heterojunction to achieve high photocatalytic antibiotic removal under visible-light irradiation. *Sep. Purif. Technol.* **2022**, *292*, 121028.
40. Alshammari, A.H.; Alshammari, M.; Alshammari, K.; Allam, N.K.; Taha, T. PVC/PVP/SrTiO₃ polymer blend nanocomposites as potential materials for optoelectronic applications. *Results Phys.* **2023**, *44*, 106173. [[CrossRef](#)]
41. Hosseini, A.; Faghihian, H. Application of FSM-16 impregnated by TiO₂ as an efficient photocatalyst for elimination of benzothio- phene and dibenzothiophene, adsorptive removal of degradation products by MCM-41. *J. Ind. Eng. Chem.* **2019**, *76*, 122–132. [[CrossRef](#)]
42. Zarringhadam, P.; Farhadi, S. Novel sheet-like bismuth subcarbonate-zinc ferrite (Bi₂O₂CO₃/ZnFe₂O₄) magnetically recy- clable nanocomposites: Synthesis, characterization and enhanced catalytic performance for the reduction of nitrophenols and nitroanilines. *Appl. Organomet. Chem.* **2018**, *32*, e4518. [[CrossRef](#)]
43. Cao, S.; Yu, J. g-C₃N₄-based photocatalysts for hydrogen generation. *J. Phys. Chem. Lett.* **2014**, *5*, 2101–2107. [[CrossRef](#)]
44. Wang, X.; Gong, J.; Dong, Y.; An, S.; Zhang, X.; Tian, J. Energy band engineering of hydroxyethyl group grafted on the edge of 3D g-C₃N₄ nanotubes for enhanced photocatalytic H₂ production. *Mater. Today Phys.* **2022**, *27*, 100806. [[CrossRef](#)]
45. Song, X.; Mao, W.; Wu, Y.; Wang, M.; Liu, X.; Zhou, W.; Huo, P. Fabricating carbon nitride-based 3D/0D intramolecular donor–acceptor catalysts for efficient photoreduction of CO₂. *New J. Chem.* **2022**, *46*, 20225–20234. [[CrossRef](#)]
46. Rong, X.; Qiu, F.; Rong, J.; Zhu, X.; Yan, J.; Yang, D. Enhanced visible light photocatalytic activity of W-doped porous g-C₃N₄ and effect of H₂O₂. *Mater. Lett.* **2016**, *164*, 127–131. [[CrossRef](#)]
47. Metin, Ö.; Özkar, S. Hydrogen generation from the hydrolysis of sodium borohydride by using water dispersible, hydrogenphosphate-stabilized nickel (0) nanoclusters as catalyst. *Int. J. Hydrogen Energy* **2017**, *32*, 1707–1715. [[CrossRef](#)]
48. Saka, C.; Balbay, A. Influence of process parameters on enhanced hydrogen generation via semi-methanolysis and semi-ethanolysis reactions of sodium borohydride using phosphoric acid. *Int. J. Hydrogen Energy* **2019**, *44*, 30119–30126. [[CrossRef](#)]
49. Xu, D.; Zhang, Y.; Guo, Q. Research progress on catalysts for hydrogen generation through sodium borohydride alcoholysis. *Int. J. Hydrogen Energy* **2021**, *47*, 5929–5946. [[CrossRef](#)]
50. Demirci, S.; Sunol, A.K.; Sahiner, N. Catalytic activity of amine functionalized titanium dioxide nanoparticles in methanolysis of sodium borohydride for hydrogen generation. *Appl. Catal. B Environ.* **2020**, *261*, 118242. [[CrossRef](#)]
51. Hannauer, J.; Demirci, U.B.; Pastor, G.; Geantet, C.; Herrmann, J.M.; Miele, P. Hydrogen release through catalyzed methanolysis of solid sodium borohydride. *Energy Environ. Sci.* **2010**, *3*, 1796–1803. [[CrossRef](#)]
52. Kassem, A.A.; Abdelhamid, H.N.; Fouad, D.M.; Ibrahim, S.A. Metal-organic frameworks (MOFs) and MOFs-derived CuO@C for hydrogen generation from sodium borohydride. *Int. J. Hydrogen Energy* **2019**, *44*, 31230–31238. [[CrossRef](#)]
53. Saka, C. g-C₃N₄ particles with boron and oxygen dopants/carbon vacancies for efficient dehydrogenation in sodium borohydride methanolysis. *Int. J. Hydrogen Energy* **2022**, *47*, 19016–19026. [[CrossRef](#)]
54. Cline, E.D.; Adamson, S.E.; Bernhard, S. Homogeneous Catalytic System for Photoinduced Hydrogen Production Utilizing Iridium and Rhodium Complexes. *Inorg. Chem.* **2008**, *47*, 10378–10388. [[CrossRef](#)] [[PubMed](#)]
55. Yang, L.; Fan, C.; Zhang, J.; Zhang, F.; Li, R.; Yi, S.; Sun, Y.; Dong, H. Poly(acrylic acid)-modified silica nanoparticles as a nonmetal catalyst for NaBH₄ methanolysis. *Int. J. Hydrogen Energy* **2021**, *46*, 23236–23244. [[CrossRef](#)]
56. Dai, P.; Yao, Y.; Hu, E.; Xu, D.; Li, Z.; Wang, C. Self-assembled ZIF-67@graphene oxide as a cobalt-based catalyst precursor with enhanced catalytic activity toward methanolysis of sodium borohydride. *Appl. Surf. Sci.* **2021**, *546*, 149128. [[CrossRef](#)]
57. Wang, F.; Luo, Y.; Zhang, Y.; Wang, Y.; Zhu, H. Preparation of bush-like Ru/NiO-Ni foam catalyst and its performance in hydrogen production from sodium borohydride alcoholysis. *Energy Fuels* **2020**, *34*, 11365–11372. [[CrossRef](#)]

Disclaimer/Publisher’s Note: The statements, opinions and data contained in all publications are solely those of the individual author(s) and contributor(s) and not of MDPI and/or the editor(s). MDPI and/or the editor(s) disclaim responsibility for any injury to people or property resulting from any ideas, methods, instructions or products referred to in the content.